aerospace

Article

An Optimized Pressure-Based Method for Thrust Vectoring Angle Estimation

Nanxing Shi , Yunsong Gu *, Tingting Wu, Yuhang Zhou, Yi Wang and Shuai Deng

Key Laboratory of Unsteady Aerodynamics and Flow Control, Ministry of Industry and Information Technology, Nanjing University of Aeronautics and Astronautics, Yudao Street 29, Nanjing 210016, China; shinanxing@nuaa.edu.cn (N.S.); wtting@nuaa.edu.cn (T.W.); zhouyuhang@nuaa.edu.cn (Y.Z.); yiiwang@nuaa.edu.cn (Y.W.); sx2201007@nuaa.edu.cn (S.D.)

* Correspondence: yunsonggu@nuaa.edu.cn

Abstract: This research developed a pressure-based thrust vectoring angle estimation method for fluidic thrust vectoring nozzles. This method can accurately estimate the real-time in-flight thrust vectoring angle using only wall pressure information on the inner surface of the nozzle. We proposed an algorithm to calculate the thrust vectoring angle from the wall pressure inside the nozzle. Non-dominated sorting genetic algorithm II was applied to find the optimal sensor arrays and reduce the wall pressure sensor quantity. Synchronous force and wall pressure measurement experiments were carried out to verify the accuracy and real-time response of the pressure-based thrust vectoring angle estimation method. The results showed that accurate estimation of the thrust vectoring angle can be achieved with a minimum of three pressure sensors. The pressure-based thrust vectoring angle estimation method proposed in this study has a good prospect for engineering applications; it is capable of accurate real-time in-flight monitoring of the thrust vectoring angle. This method is important and indispensable for the closed-loop feedback control and aircraft attitude control of fluidic thrust vectoring control technology.

Keywords: passive fluidic thrust vectoring control; thrust vectoring angle estimation; genetic algorithm optimization; pressure distribution reconstruction; non-dominated sorting genetic algorithm II

check for updates

Citation: Shi, N.; Gu, Y.; Wu, T.; Zhou, Y.; Wang, Y.; Deng, S. An Optimized Pressure-Based Method for Thrust Vectoring Angle Estimation. *Aerospace* **2023**, *10*, 978. https://doi.org/10.3390/aerospace10120978

Academic Editor: Christian Breitsamter

Received: 16 October 2023
Revised: 16 November 2023
Accepted: 16 November 2023
Published: 22 November 2023

1. Introduction

Thrust vectoring control (TVC) is an indispensable technology for the next-generation high-performance fighter. It can partly replace aerodynamic rudders to provide aircraft attitude control force [1], significantly enhance the maneuverability and agility of the aircraft, and improve aerial combat capabilities. TVC methods can be divided into two categories: mechanical thrust vectoring control and fluidic thrust vectoring control (FTVC). Mechanical thrust vectoring control changes the shape of the nozzle to limit or change the flow direction of the jet. It can achieve continuous and stable control of the jet vectoring direction but with disadvantages such as complex and heavy mechanical structures, slow jet vectoring response, and thrust loss [2]. In contrast, FTVC can avoid some of these problems. FTVC changes the flow direction of the jet using active flow control methods, thus avoiding complex mechanical structures. Some typical FTVC methods include shock vector control [3–5], throat shifting control [6,7], dual throat control [8–10], counterflow control [11,12], and co-flow control [13,14]. These FTVC methods all use air sources, such as high-pressure air tanks or engine bleed air, to generate an active secondary flow, which will add redundant structures to the control system of the nozzle. Therefore, these methods are defined as *active* FTVC. In our study, we investigated a *passive* FTVC nozzle, which only consists of two bilateral inclined offset walls and a pair of secondary flow valves [15]. There is no need for an air source, high-pressure device, or engine bleed air to generate an active secondary flow. Due to the advantages of low energy consumption, fast deflection speed, and low thrust loss, passive FTVC is very promising for engineering applications.

The thrust vectoring angle is a key performance indicator of TVC technology, which not only affects the thrust of the engine but also determines the magnitude of the normal force generated by the TVC system. When the TVC system is used as an aerodynamic rudder, thrust vectoring angle directly affects the attitude maneuvering torque of the aircraft. Moreover, if closed-loop feedback control of the nozzle is required, it is necessary to obtain the in-flight real-time thrust vectoring angle. Therefore, real-time in-flight monitoring of the thrust vectoring angle generated by the TVC system is very important. Mechanical thrust vectoring control can indirectly obtain the vectoring angle of the jet through the deflection degree of the nozzle configuration. Unfortunately, there is no efficient way for FTVC methods to acquire the in-flight thrust vectoring angle. In ground performance tests, the vectoring angle of the FTVC system is usually measured by the balance system or the particle image velocimetry (PIV) system [16]. Flamm [17] used a six-component strain gauge balance to obtain the thrust vectoring characteristics of a fluidic counterflow nozzle. PIV can acquire the flow field in space in the form of non-contact measurement [18]. Raman et al. [19] used PIV to investigate the flow structures of a jet in a miniature fluidic oscillator. However, it is difficult to directly measure the in-flight engine thrust [20]. In-flight optical non-contact measurement of the exhausted jet is also difficult and impractical. These technical bottlenecks are detrimental to the application of FTVC technologies and need to be addressed urgently. Therefore, this investigation proposes a method for estimating the thrust vectoring angle based on wall pressure distribution, which makes it possible to acquire the in-flight thrust vectoring angle of the FTVC system. Unlike the previously existing balance measurement and PIV methods, the strategy proposed in this study only requires a few sparse pressure measurement points inside the FTVC nozzle, combined with our vectoring angle solving algorithm, to realize the real-time static and dynamic measurement of the jet vectoring angle.

In aerodynamics, the estimations of aerodynamic properties from the surface pressure distribution have been widely used, and we expect to learn from them and propose a new pressure-based thrust vectoring angle estimation method for FTVC nozzles. For example, multi-hole probes can determine the three-dimensional velocity vector and fluid properties through the pressure data at specific locations on the head of the probe [21]. In the case of a delta wing, the instantaneous loads can be predicted from sparse pressure measurements [22]. The flush air data sensing system can use a matrix of pressure orifices on the nose of the aircraft to estimate air data parameters [23]. The lateral force caused by the bi-stable asymmetric forebody vortices at a high angle of attack can be estimated by the circumferential pressure distribution [24]. Regarding FTVC technology, previous studies have indicated that the vectoring angle of FTVC is strongly determined by the near-wall pressure on both sides of the jet [25–27]; therefore, it is possible to estimate the thrust vectoring properties through the wall pressure distribution. Normally, a dense array of pressure sensors on the nozzle wall is always required to obtain the pressure distribution on the wall, but this solution is impractical for in-flight applications. The acceptable solution is to place sparse sensors at several key locations. However, inside the FTVC nozzles, the interaction between the jet and the wall is exceptionally complicated; typical near-wall flow processes include the shear layer, reattachment, and separation bubble [28–30]. Moreover, during the transient process of jet deflection, there will be dramatic changes in the near-wall flow structures, such as the formation and breakdown of the separation bubble [31]. These circumstances determining the wall pressure distribution of the FTVC nozzle are irregular and unsteady, which makes it very difficult to find the critical pressure locations to indicate the thrust vectoring properties. Therefore, we use genetic algorithm optimization to find the optimal locations with the least sensors.

Genetic algorithms show good performance in finding the best global solution to difficult problems [32,33], and they have been widely employed in layout optimization [34–38]. However, traditional genetic algorithms are computationally expensive for large populations [38]. In this research, we used the non-dominated sorting genetic algorithm II (NSGA-II) to optimize the layout of the pressure sensors. NSGA-II was developed from

NSGA [39], which has the advantages of a fast non-dominated sorting procedure, an elitist strategy, a parameterless approach, and a simple yet efficient constraint-handling method [40]. NSGA-II is particularly suitable for solving multi-objective optimization problems because this method uses an inexpensive, low-fidelity analytical approach to evaluate objectives and constraints [41].

In summary, it is extremely important for thrust vectoring nozzles to obtain the real-time in-flight thrust vectoring angle. However, for FTVC nozzles, there is no effective way to measure the thrust vectoring angle in-flight. It is theoretically possible to obtain the thrust vectoring angle by placing hundreds or thousands of pressure sensors on the inner side wall of the nozzle, but this is obviously not practical in engineering applications. To solve this pressing problem, this research proposes an optimized pressure-based thrust vectoring angle estimation method for fluidic thrust vectoring nozzles. It is capable of monitoring the real-time in-flight thrust vectoring angle with a sparse pressure sensor array, which is optimized by a genetic algorithm. We conducted synchronous experiments to prove the accuracy and real-time response of this method. The pressure-based vectoring angle estimation method is a reliable meter for FTVC nozzles, which can provide accurate vector angles to the pilot or flight control system, thus improving the aircraft attitude control capability and safety of FTVC control. Therefore, this method is important and indispensable for the further application of FTVC technology.

This paper consists of five sections. Section 2 introduces the experimental facilities and techniques. Section 3 introduces the theory of the research and the optimization method. Section 4 discusses the results of the research. Section 5 presents the conclusions.

2. Experimental Approach

2.1. Test Facilities and Model

We built an electric jet propulsion system to investigate and validate the pressure-based thrust vectoring angle estimation method proposed in this research. The propulsion system is powered by a 144 mm ducted fan, which can generate jets with velocities ranging from 10 to 60 m/s. The type of 144 mm ducted fan is a 144EDF-Metal fan, which is manufactured by Taizhou Juxian Drone Company in China. The size of the jet outlet can be changed by replacing the contraction section. The test facilities include the pressure measurement system, the six-component balance system, and the synchronous DAQ system, as shown in Figure 1.

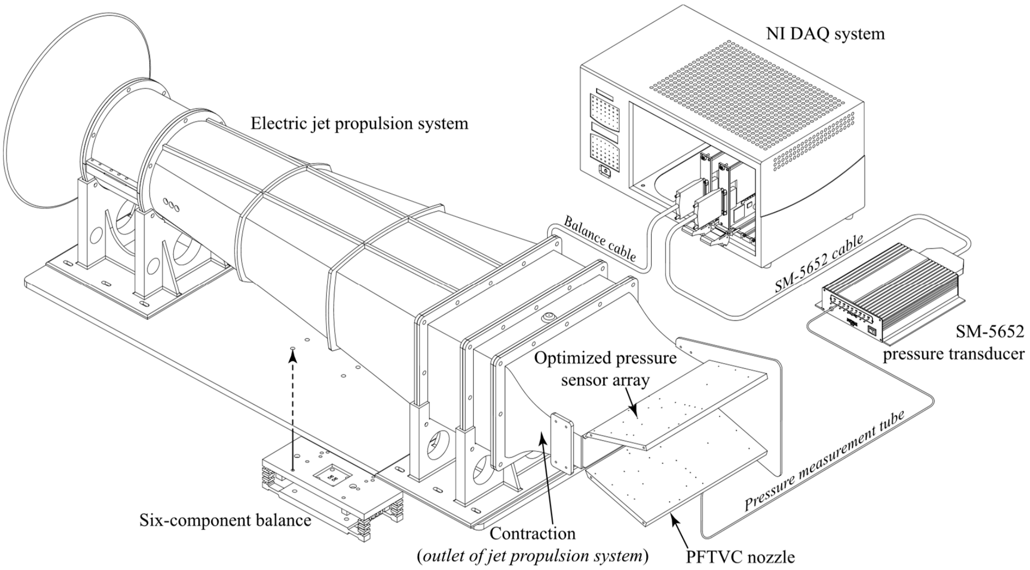

Figure 1. A schematic highlighting the salient features of the experimental facility.

The passive FTVC nozzle is installed at the outlet of the jet propulsion system to achieve jet vectoring control. The detailed parameters of the passive FTVC nozzle are illustrated in Figure 2. The main structures of the nozzle consist of two inclined walls, two sidewalls, and two control valves. The origin of the nozzle coordinate axis system is located at the center of the jet outlet, the $\boldsymbol{Y}$-axis coincides with the center axis of the jet propulsion system, the $\boldsymbol{Z}$-axis is in the opposite direction of gravity, and the $\boldsymbol{X}$-axis is determined by the right-hand rule, as shown in Figure 2a. There is an offset of G = 6 mm between the jet outlet and the leading edge of the inclined wall. The incline angle between the inclined wall and the nozzle $\boldsymbol{Y}$-axis is θ = 16°. The length of the inclined wall is L = 125 mm, and the height of the jet outlet is H = 50 mm. The two sidewalls are located on the lateral sides of the inclined wall. In Figures 1 and 2, the sidewall on the left side is hidden.

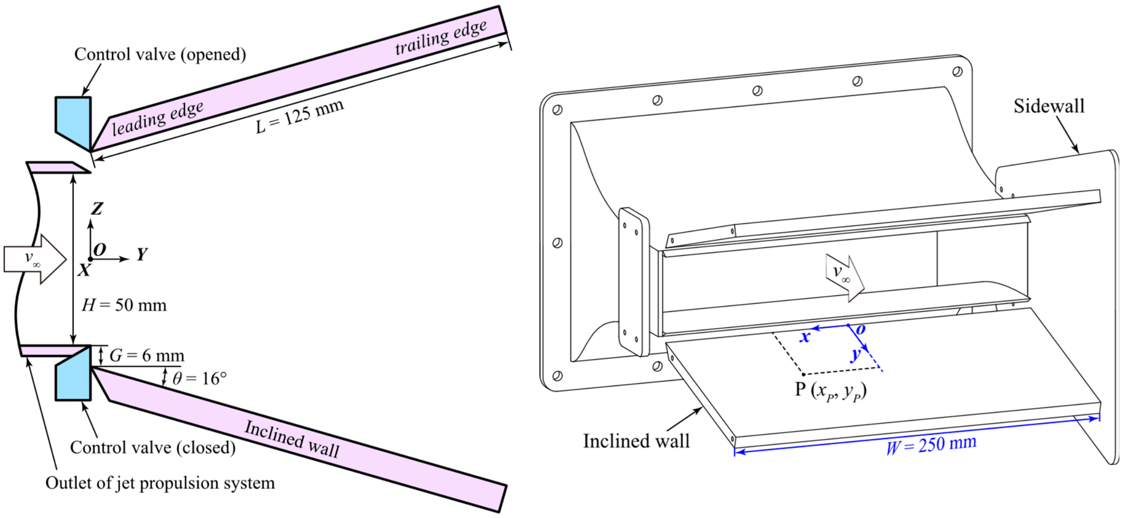

(**a**) (**b**)

Figure 2. The detailed parameters of the passive FTVC nozzle. (**a**) Side view and the nozzle coordinate axis system ***O-XYZ***. (**b**) Oblique view and the wall coordinate axis system ***o-xyz***.

To facilitate the description of the position on the inclined wall, the wall coordinate axis system shown in Figure 2b is defined. Take the inclined wall on the lower side as an example; the coordinate origin $\boldsymbol{o}$ is located at the center of the leading edge of the inclined wall, the $\boldsymbol{x}$-axis points to the left along the leading edge of the wall (transverse), and the $\boldsymbol{y}$-axis points to the trailing edge along the wall (streamwise). The width of the jet outlet is W = 250 mm.

2.2. Pressure Measurement System

The pressure measurement system was used to obtain the pressure distribution on the inclined wall during jet vectoring control. It has 64 acquisition channels using SM-5652 pressure transducers, which were manufactured by Silicon Microstructures Incorporated (SMI) in the USA. Data were acquired using a NI PXI-6284 multifunction I/O module. The measurement range is 0.15 PSI, and the precision is 0.05% F.S. According to the feature of the differential pressure sensor, the pressure can be expressed by

$$P_{test} = P_s - P_{atm}, \tag{1}$$

$$C_p = \frac{P_{test}}{\frac{1}{2}\rho v_\infty^2}, \tag{2}$$

where P_{test} is the pressure acquired by the sensor, P_s is the local absolute pressure, P_{atm} is the atmospheric pressure at the reference of the sensor, C_p is the pressure coefficient, ρ is the density of the air, and v_∞ is the velocity of the jet at the outlet.

2.3. Six-Component Balance System

The six-component balance system was used to directly measure the thrust vectoring characteristics during jet deflection, thus verifying the accuracy of the pressure-based thrust vectoring angle estimation. The balance system consists of the six-component balance, one NI PXI-6284 multifunction I/O module, and one NI PXIe-1078 computer. The six-component balance (type GYS-TP-01-B1) was built in-house; it contains a total of 28 resistive strain gauges, 8 in the F_Y direction and 4 in each of the other directions. The type of the strain gauges is BF350, which were manufactured by AVIC Zhonghang Electronic Measuring Instruments Company in China. The specifications of the balance are shown in Table 1, and the balance axes are the same as the nozzle coordinate axis system in Figure 2a.

Table 1. Specifications of the six-component balance.

	F_X	F_Y	F_Z	M_X	M_Y	M_Z
Range (kg, kg·m)	15	3	20	2	1	1
Accuracy (%F.S.)	0.32	0.44	0.17	0.42	0.38	0.26
Precision (%F.S.)	0.07	0.18	0.08	0.10	0.12	0.09

2.4. Synchronous DAQ System

The synchronous DAQ system was used to enable the time-synchronous acquisition of forces and wall pressure distribution during thrust vector control in Section 4.5. The DAQ system consists of one NI PXIe-1078 computer and two NI PXI-6284 multifunction I/O modules, which were manufactured by National Instruments (NI) in Texas, USA. The synchronous acquisition software was programmed based on NI LabVIEW. The force signals acquired by the balance system were used for a direct calculation of the thrust vectoring angle, and the pressure signals collected by the pressure sensors were used for an indirect estimation of the thrust vectoring angle. The schematic diagram of the synchronous DAQ system is shown in Figure 3. The pressure measurement system and the balance system acquire data simultaneously and continuously at a sampling frequency of 100 Hz. At moment t_1, the control valve actuates the jet to deflection until moment t_2, as illustrated by the pink rectangular area. The reliability of the pressure-based thrust vectoring angle estimation algorithm can be demonstrated by comparing its difference with the vectoring angle directly measured by the balance at the same moment.

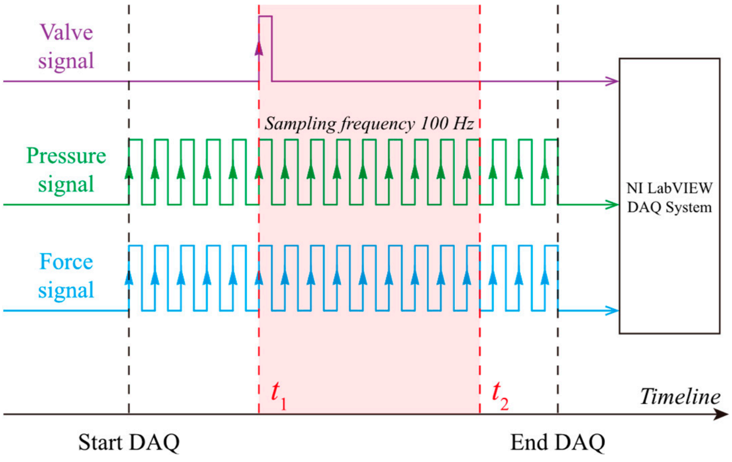

Figure 3. Timing chart of the synchronous DAQ system.

3. Methodology

3.1. Passive Fluidic Thrust Vectoring Control

This section briefly describes the basic control principles of passive FTVC. As mentioned previously, there is no need for an air source, high-pressure device, or engine bleed air for passive FTVC to deflect the jet. As shown in Figure 4a, the shear layer of the primary jet keeps entraining fluid into the primary jet, which makes the pressure in the near-wall area of the nozzle lower than the external pressure of the environment. Because both the upper and lower valves are opened, the ambient fluid will be passively entrained into the nozzle from the environment through the secondary flow channel. In this case, the flow conditions of the upper and lower sides of the jet are basically the same, and the jet is neutral. When one of the valves is closed, such as the lower side shown in 0b, the passive secondary flow on the lower side will be cut off. Then, a strong low-pressure area will be created in the near-wall region on the lower side, actuating the jet to deflect towards the lower side. Figure 4b also provides the typical wall pressure distribution of the attached jet [31], which shows that there is a low-pressure region near the leading edge of the wall. By changing the closure percentage of the control valves, the jet can be deflected at different vectoring angles. The closure percentage δ_v of the valves is defined as

$$\delta_v = \frac{S}{S_{max}}, \tag{3}$$

where $S_{max} = G \times W$, which is the maximum cross-sectional area of the secondary flow channel, and S is the area blocked by the control valve.

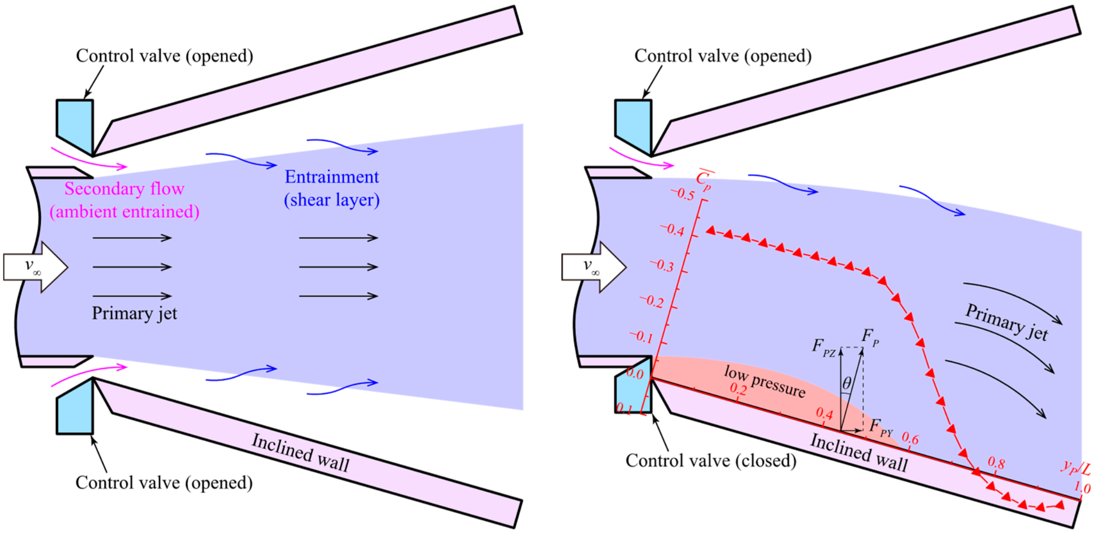

(**a**) (**b**)

Figure 4. The basic control principles of passive FTVC. (**a**) Neutral detached jet. (**b**) Attached jet and the wall pressure distribution of the wall on the downside [31].

3.2. Thrust Vectoring Angle Algorithm Based on Wall Pressure Distribution

According to [13], the thrust vectoring angle generated by the TVC system can be calculated by

$$\theta_T = \arctan\frac{F_Z}{F_Y}, \tag{4}$$

where θ_T is the thrust vectoring angle and F_Y and F_Z are the axial force in the $\boldsymbol{Y}$-direction and the normal force in the $\boldsymbol{Z}$-direction, respectively.

In Strykowski's [42] study on a counterflow TVC nozzle, he proposed a method to calculate thrust vectoring angle from wall pressure

$$\theta_P = \arcsin\frac{(P_\infty - P_B)L}{J}, \tag{5}$$

where θ_P is the thrust vectoring angle estimated by pressure, P_∞ is the local ambient pressure, P_B is the pressure at the secondary flow channel, L is the length of the wall, and J is the forward momentum of the jet.

The method in Equation (5) uses the pressure of the secondary flow channel to represent the overall pressure of the wall, but the actual wall pressure distribution is not uniform. In addition, it ignores the wall incline angle and the effect of backpressure on thrust. Therefore, the thrust vectoring angle calculated by this method is inaccurate.

In this investigation, we propose a thrust vectoring angle algorithm based on wall pressure. The thrust generated by the jet is

$$T_{jet} = \dot{m}v_\infty + S_e(P_e - P_{atm}), \tag{6}$$

$$T_{jet} = \rho v_\infty^2 HW + HW(P_e - P_{atm}), \tag{7}$$

where $\dot{m}$ is the mass flow of the jet, S_e is the area of the jet outlet, P_e is the static pressure of the jet at the outlet, P_{atm} is the environmental pressure, and ρv_∞^2 is the dynamic pressure, which can be measured at the jet outlet.

When the vectoring angle of the jet is θ_P, the thrust component of T_{jet} in the $\boldsymbol{Y}$-direction is

$$T_{Y,jet} = HW\left(\rho v_\infty^2 + P_e - P_{atm}\right)\cos\theta_P. \tag{8}$$

The normal force generated by the passive FTVC system is calculated from the wall pressure distribution. As shown in Figure 4b, the resultant force applied on the lower wall by the negative pressure is F_P, which can be calculated by

$$F_P = -\iint \frac{1}{2}\rho v_\infty^2 C_p(x,y)dxdy, \tag{9}$$

$$F_P = -\overline{C_p}\frac{1}{2}\rho v_\infty^2 S_w, \tag{10}$$

where $\overline{C_p}$ is the average wall pressure coefficient all over the wall and $S_w = W \times L$ is the area of the inclined wall.

As shown in Figure 4b, the component of F_P in the $\boldsymbol{Z}$-direction is

$$F_{PZ} = -\frac{1}{2}\rho v_\infty^2 WL\overline{C_p}\cos\theta. \tag{11}$$

As a result, the thrust vectoring angle θ_P estimated by pressure distribution can be calculated by

$$\tan\theta_P = \frac{F_{PZ,lower} - F_{PZ,upper}}{T_{Y,jet}}, \tag{12}$$

$$\frac{\sin\theta_P}{\cos\theta_P} = \frac{\rho v_\infty^2 WL\cos\theta}{2HW(\rho v_\infty^2 + P_e - P_{atm})\cos\theta_P}\left(\overline{C_{p,upper}} - \overline{C_{p,lower}}\right), \tag{13}$$

$$\theta_P = \arcsin\left[\frac{\rho v_\infty^2 L\cos\theta}{2H(\rho v_\infty^2 + P_e - P_{atm})}\left(\overline{C_{p,upper}} - \overline{C_{p,lower}}\right)\right]. \tag{14}$$

From Equation (14), it can be seen that the average wall pressure plays a key role in pressure-based thrust vectoring angle estimation. For this reason, we need to obtain the pressure distribution over the inclined wall. However, placing hundreds or thousands of pressure sensors on the wall is impractical. Therefore, we employed NSGA-II to achieve the reduction in sensor quantity and optimization of the sensor array.

In this research, we used two strategies to estimate the average wall pressure:

1. Pressure distribution reconstruction method: Reconstruct the wall pressure distribution from sparse sensor arrays on the wall and then obtain the average wall pressure. The reconstruction methods include 2D reconstruction (Section 4.1), 3D reconstruction (Section 4.2), and half-3D reconstruction (Section 4.3);
2. Direct average pressure method: Characterize the average wall pressure directly using the average pressure of the sparse pressure sensors (Section 4.4).

The strategies and objectives of different methods are shown in Table 2.

Table 2. The strategies and objectives of different methods.

Method	Section	Equations	Strategy	Goal
2D	4.1	(14) (26)	Pressure distribution reconstruction	Thrust vectoring angle estimation
3D Half-3D	4.2 4.3	(14) (28)		
Aver C_p	4.4	(14) (30)	Direct average pressure	

3.3. NSGA-II Optimization Method

This section introduces the optimization process of the sensor layout based on NSGA-II and the accuracy verification of the pressure-based thrust vectoring angle estimation method based on wall pressure distribution proposed in this paper. The procedure of the investigation can be described as follows:

1. Obtain the original wall pressure distributions at different δ_v using a dense array of pressure sensors;
2. Define the number of the sensors (N_s) and the optional position ranges of the sensors for optimization;
3. NSGA-II optimization (flow chart shown in Figure 5);
4. Carry out the synchronous force and pressure measurement experiment shown in Figure 1 to verify the accuracy and dynamic response performance of pressure-based thrust vectoring angle estimation.

The mean absolute error ε and the mean relative error ε_r are defined as

$$\varepsilon = \frac{1}{N}\sum\nolimits_{i=1}^{N} |x^* - x_{real}|, \tag{15}$$

$$\varepsilon_r = \frac{\varepsilon}{\overline{x_{real}}} \times 100\%. \tag{16}$$

The root mean square error (RMSE) and the relative root mean square error (RRMSE) are used for the evaluation of the optimization results which, according to ref. [43], can be defined as

$$RMSE = \sqrt{\frac{1}{N}\sum\nolimits_{i=1}^{N} (x^* - x_{real})^2}, \tag{17}$$

$$RRMSE = \frac{RMSE}{\overline{x_{real}}} \times 100\%. \tag{18}$$

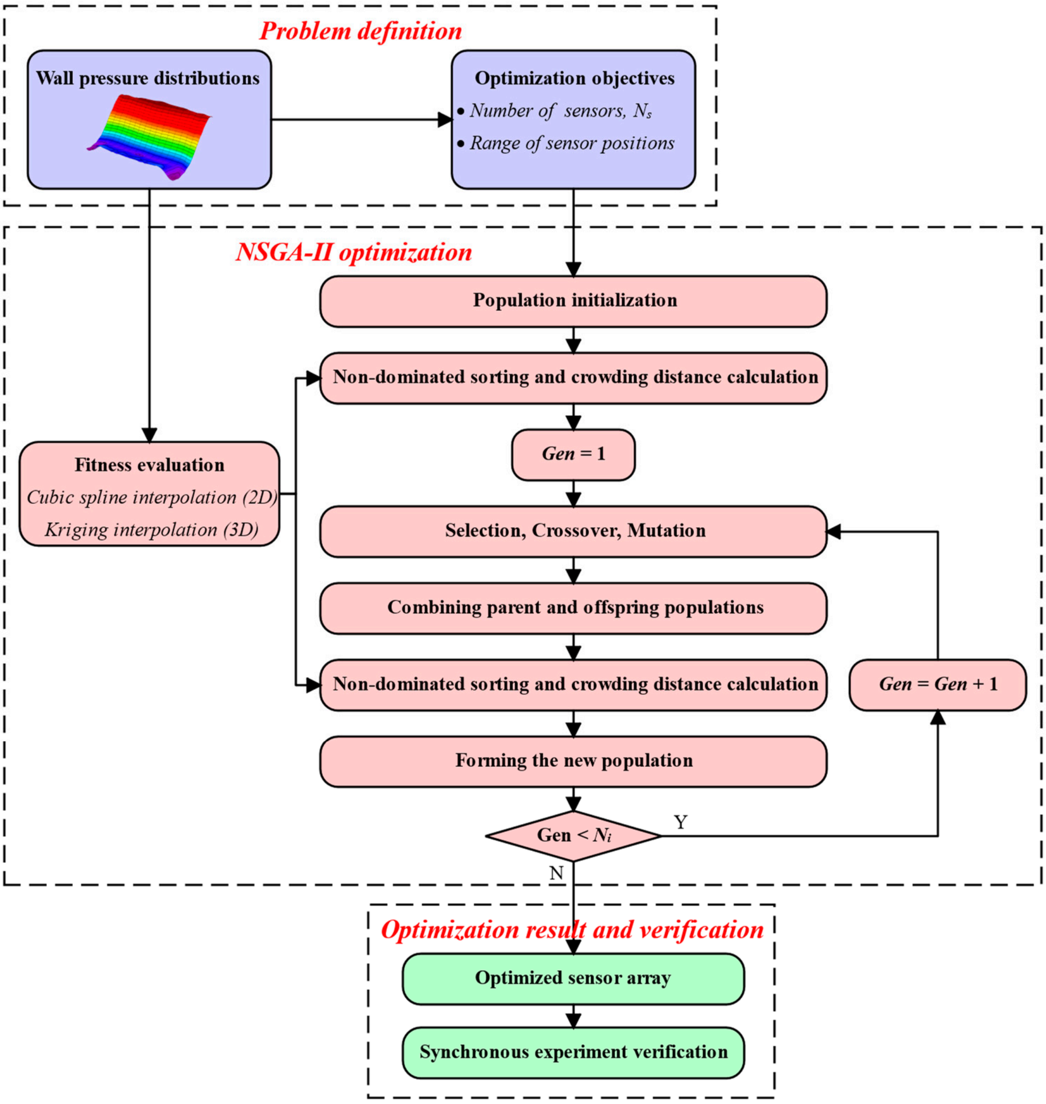

Figure 5. Flow chart of the NSGA-II optimization method.

3.4. Kriging Interpolation

Kriging is a well-known spatial interpolation method that has been applied in various research studies [44,45]. Kriging was named by Matheron [46] after Krige [47], who pioneered this method for determining ore-grade distributions based on core samples. The Kriging method can use the initial set of data values to perform optimal and unbiased estimates of regionalized variables at unsampled locations [48]. In this research, we use Kriging interpolation to reconstruct the overall wall pressure distributions of the 3D jets from sparse pressure data.

In the estimation of Kriging interpolation coefficients, a semi-variogram is introduced to measure the spatial correlation of the sample data with distance. Suppose that $z(s)$ is the value at point s and $z(s + h)$ represents the value spacing distance h apart; then, the semi-variogram of $z(s)$ is defined as [49]

$$r(h) = \frac{1}{2} Var[z(s) - z(s+h)]. \tag{19}$$

The Gaussian semi-variogram model is used; the theoretical semi-variogram is

$$r(h) = C_0 + C\left[1 - \exp\left(-h^2/a^2\right)\right], \tag{20}$$

where C_0 is the nugget effect, C is the structured variance, and a is the variogram range.

With the original values $z(s_1)$, $z(s_2)$, …, $z(s_n)$ at points s_1, s_2, …, s_n, the Kriging estimation of the unsampled position s_0 is [49]

$$\hat{z}(s_0) = \sum_{i=1}^{n} \lambda_i z(s_i), \tag{21}$$

where λ_i is chosen to ensure that the estimation is unbiased and the variance of the estimation error is minimum; the optimization objective can be expressed as [49]

$$\min\left\{ Var\left[z(s_0) - \sum_{i=1}^{n} \lambda_i z(s_i)\right] - 2m\left(\sum_{i=1}^{n} \lambda_i - 1\right)\right\}, \tag{22}$$

where m is a Lagrange multiplier that ensures $\sum_{i=1}^{n} \lambda_i = 1$. Then, λ_i can be obtained from [49,50]

$$-\sum_{j=1}^{n} \lambda_j r(s_i - s_j) + r(s_0 - s_i) - m = 0. \tag{23}$$

Equation (23) can be written as:

$$\begin{pmatrix} r_{11} & \cdots & r_{1n} & 1 \\ \vdots & \ddots & \vdots & \vdots \\ r_{n1} & \cdots & r_{nn} & 1 \\ 1 & \cdots & 1 & 0 \end{pmatrix} \begin{pmatrix} \lambda_1 \\ \vdots \\ \lambda_n \\ m \end{pmatrix} = \begin{pmatrix} r_{01} \\ \vdots \\ r_{0n} \\ 1 \end{pmatrix}, \tag{24}$$

where $r_{ij} = r(s_i - s_j)$. By solving this system of equations, the value at the unsampled position s_0 can be estimated.

4. Results and Discussion

First, we define the optimization objectives and parameters for different pressure distribution reconstruction methods and average pressure estimation methods, as shown in Table 3.

Table 3. Optimization parameters for different pressure distribution reconstruction and average pressure estimation methods.

Method	Section	Range	Population	Iteration N_i	Number of Sensors N_s	Objective
2D	4.1	$\begin{cases} x_P = 0 \\ 5 \le y_P \le 120 \end{cases}$	200	400	2~24	Optimal reconstruction of wall pressure distribution
3D	4.2	$\begin{cases} -120 \le x_P \le 120 \\ 5 \le y_P \le 120 \end{cases}$	500	800	1~24	
Half-3D	4.3	$\begin{cases} 0 \le x_P \le 120 \\ 5 \le y_P \le 120 \end{cases}$				
Aver C_p	4.4	$\begin{cases} 0 \le x_P \le 120 \\ 5 \le y_P \le 120 \end{cases}$	500	800	1~24	Optimal estimation of average wall pressure

4.1. Optimal Reconstruction of 2D Wall Pressure Distribution

In this section, the 2D jet in the transverse symmetry plane ***YOZ*** is studied without considering the three-dimensional characteristics of the jet.

4.1.1. Original Wall Pressure Distributions of 2D Jets

For the 2D jet in the plane shown in Figure 6, we set 24 equally spaced pressure taps on the wall from the leading edge to the trailing edge to obtain the real wall pressure distributions of the 2D jet. The positions of the pressure taps for the 2D jet can be described as

$$\begin{cases} x_{Pi} = 0, \\ y_{Pi} = 5i,\ i = 1, 2, \cdots, 24. \end{cases} \tag{25}$$

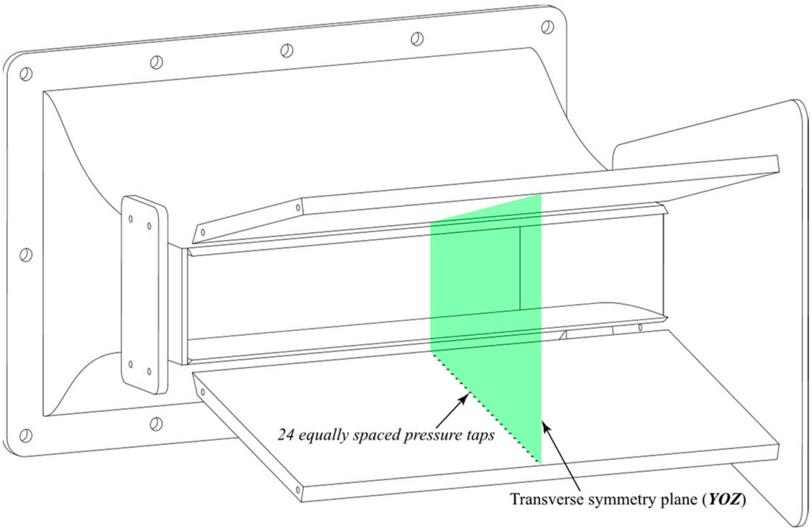

Figure 6. Distribution of original pressure measurement taps for the 2D jet in the transverse symmetry plane ***YOZ***.

Figure 7 shows the original wall pressure distributions of the 2D jets under different δ_v values. There are two main patterns of pressure distribution. In the first case, the pressure over the wall is basically uniform from the leading edge to the trailing edge (δ_v = 0~0.2 in Figure 7), which corresponds to the detached jet shown in Figure 4a. In the second case, the pressures at the wall's leading edge and trailing edge show a significant difference (δ_v = 0.4~1 in Figure 7), which corresponds to the attached jet shown in Figure 4b. The variation in the wall pressure distribution characteristics is due to the different near-wall flow structures [31]. Therefore, the sparse pressure sensors distributed on the wall should have the ability to optimally fit the wall pressure distribution under different δ_v values.

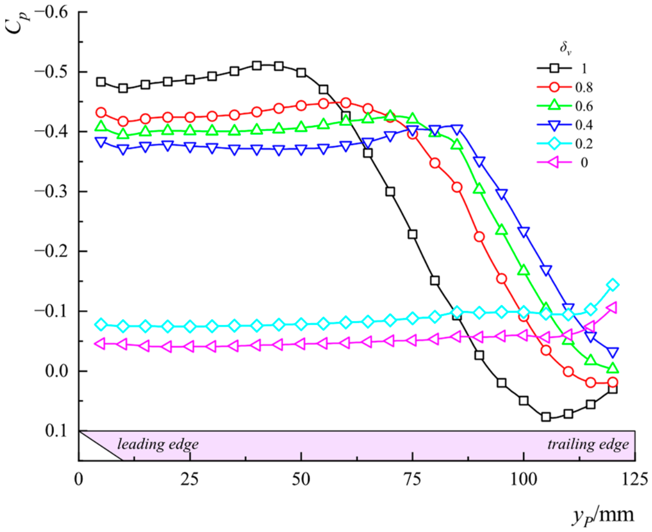

Figure 7. The original wall pressure distributions of 2D jets under different δ_v values.

4.1.2. Optimization Results and Performance of 2D Wall Pressure Distribution Reconstruction

The optimal pressure reconstruction errors of different iterations are shown in Figure 8a. When N_i = 400, the error has been minimized and smoothed. Figure 8b shows the pressure reconstruction errors of different N_s. In general, the greater the number of sensors, the smaller the error in reconstructing the pressure distribution. The error decreases with a turn at N_s = 6, and the error is basically smooth when N_s > 6. Therefore, in the case of a 2D jet, N_s = 6 provides the best balance between improvement of reconstruction accuracy and reduction of sensor quantity.

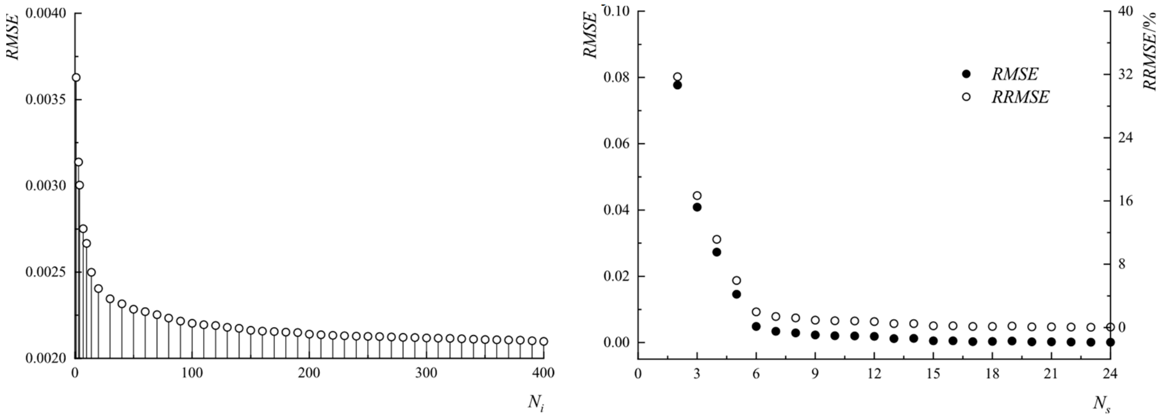

(**a**) (**b**)

Figure 8. The 2D pressure distribution reconstruction error. (**a**) Error of 400 iterations. (**b**) Error of different numbers of sensors N_s.

Figure 9 shows the optimized 2D pressure distribution reconstruction performance with different numbers of sensors. For the cases of detached jets (e.g., δ_v = 0), only a few sensors are required to provide good pressure reconstruction results because the pressure distribution is relatively uniform. However, when it comes to the cases of attached jets (e.g., δ_v = 0.5 and 1), reconstruction of the wall pressure distribution appears unsatisfactory when N_s < 6 (see Figure 9a,b). When N_s = 6, Figure 9c shows that under different δ_v values, the reconstructed pressures match well with the real pressure distributions. From the comparison of Figure 9c,d, it can be seen that the pressure reconstruction performance of six or more sensors is nice and basically consistent. Therefore, for 2D jets, the optimal number of sensors is six.

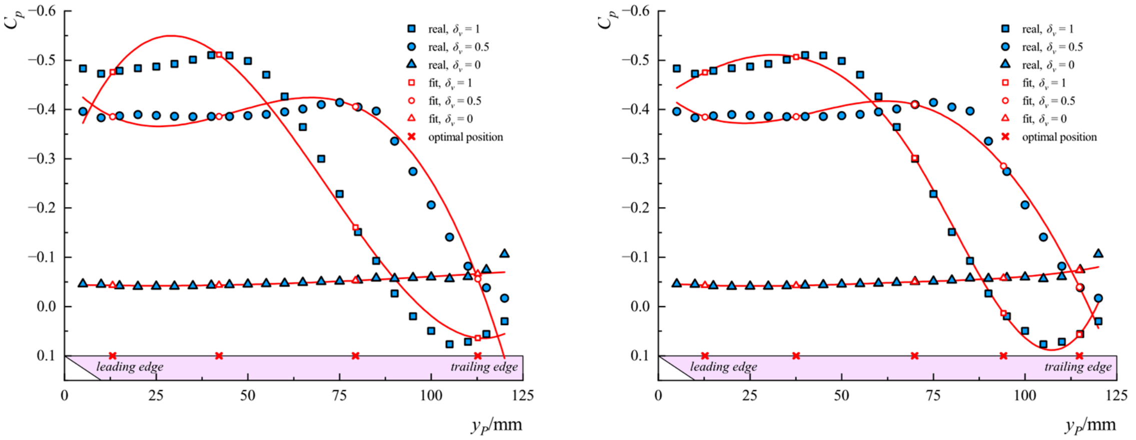

(**a**) (**b**)

Figure 9. *Cont.*

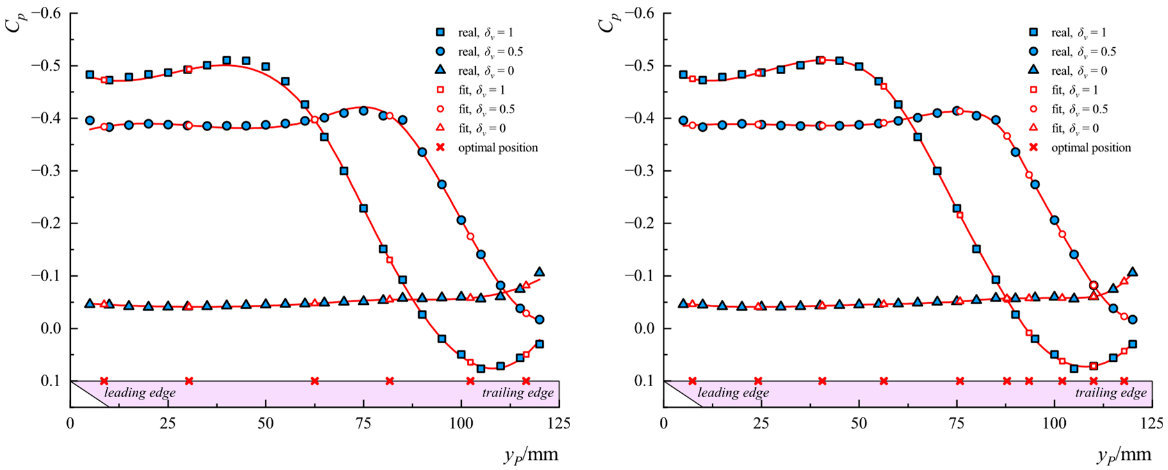

(**c**) (**d**)

Figure 9. Optimized 2D pressure distribution reconstruction performance of different numbers of sensors. (**a**) N_s = 4. (**b**) N_s = 5. (**c**) N_s = 6. (**d**) N_s = 10.

With the reconstructed pressure distribution, the average wall pressure of a 2D jet is

$$\overline{C_p} = \frac{1}{L}\int C_p(y)dy, \tag{26}$$

where C_p (y) is the reconstructed 2D pressure distribution function.

4.2. Optimal Reconstruction of 3D Wall Pressure Distribution

In this section, the overall wall pressure distribution of the jet is researched, and the three-dimensional pressure characteristics of the jet are taken into consideration.

4.2.1. Original Wall Pressure Distributions of 3D Jets

We arranged a 24 × 25 pressure sensor array to measure the original 3D wall pressure distributions of the jet, as shown in Figure 10. The positions of the pressure taps can be described as

$$\begin{cases} x_{Pij} = 5(j-1), j = 1,2,\cdots,25, \\ y_{Pij} = 5i,\ i = 1,2,\cdots,24. \end{cases} \tag{27}$$

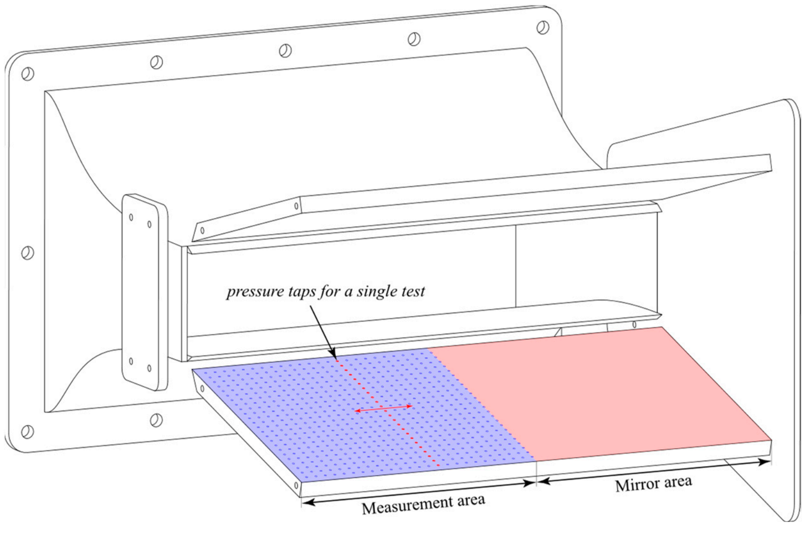

Figure 10. Distribution of original pressure measurement taps for the 3D jet.

Because there are a total of 600 pressure measurement locations and the limit of pressure channels is 64, we obtained only one column of pressure data in a single run, and the overall pressure distribution in the measurement area could be acquired through multiple scans, as illustrated by the blue area in Figure 10. The jet can be considered symmetrical in the transverse direction, so the pressure of the wall where $x > 0$ is measured as well as the region where $x < 0$ is the mirror area, as illustrated by the pink area in Figure 10.

Figure 11 provides the original 3D wall pressure distribution of the jets under different δ_v values. Similar to the case of 2D jets, the 3D wall pressure distribution also has two distribution patterns. The first pattern corresponds to a detached jet, such as Figure 11d, which has a very flat wall pressure distribution with no obvious transverse pressure differences. The second pattern corresponds to an attached jet, such as Figure 11a–c, where the pressure is low at the leading edge and high at the trailing edge. However, unlike the 2D jets, in the cases of the attached 3D jets, there is a transverse difference in pressure distribution in the two corner areas of the leading edge, as shown in Figure 11a. According to this phenomenon, the wall pressure distribution is divided into a 2D region and 3D region.

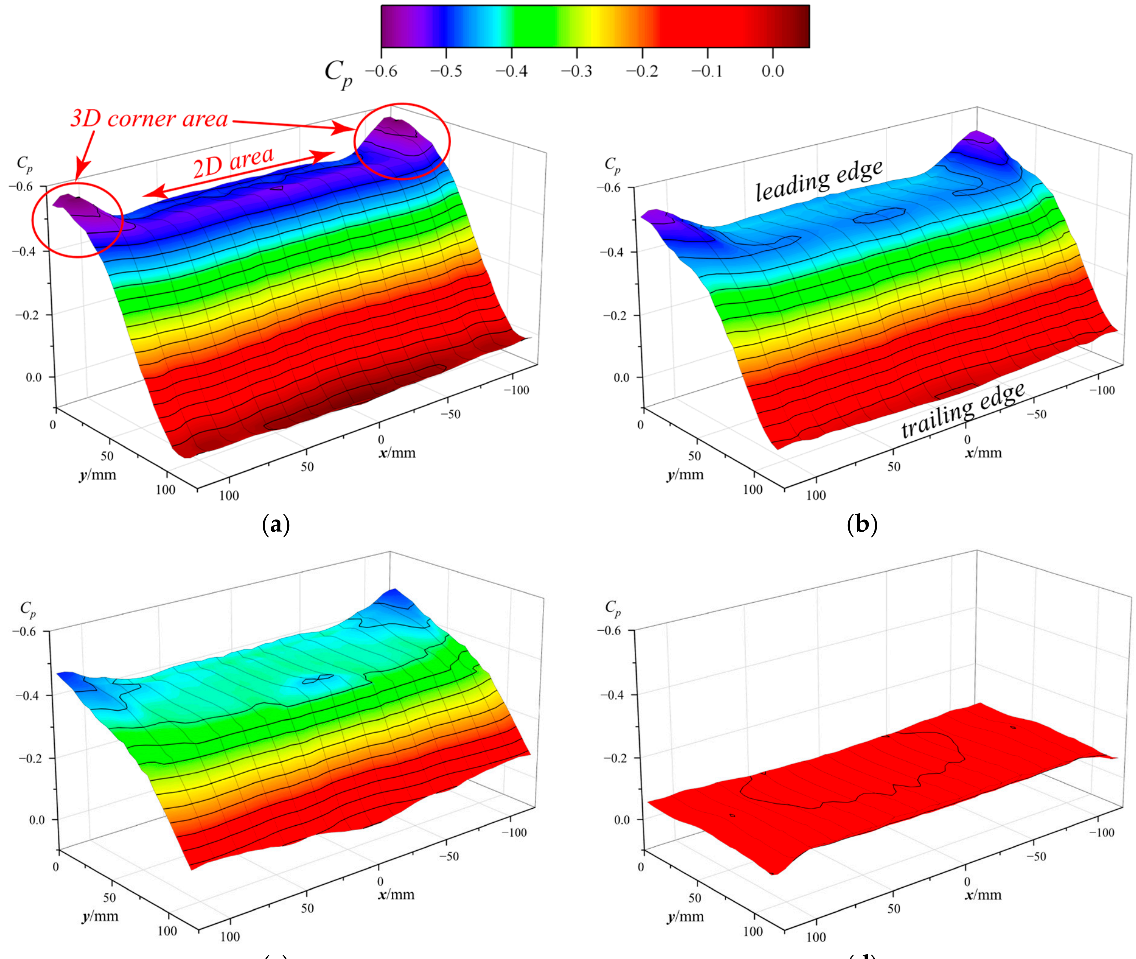

(**a**)

(**b**)

(**c**)

(**d**)

Figure 11. The original wall pressure distributions of 3D jets under different δ_v values. (**a**) $\delta_v = 1$. (**b**) $\delta_v = 0.8$. (**c**) $\delta_v = 0.5$. (**d**) $\delta_v = 0$.

4.2.2. Optimization Results and Performance of 3D Wall Pressure Distribution Reconstruction

The 3D pressure distribution reconstruction error of different N_s amounts is shown in Figure 12. Because the 3D wall pressure distribution is much more complex than the 2D case, the reconstruction error becomes larger compared with the 2D case.

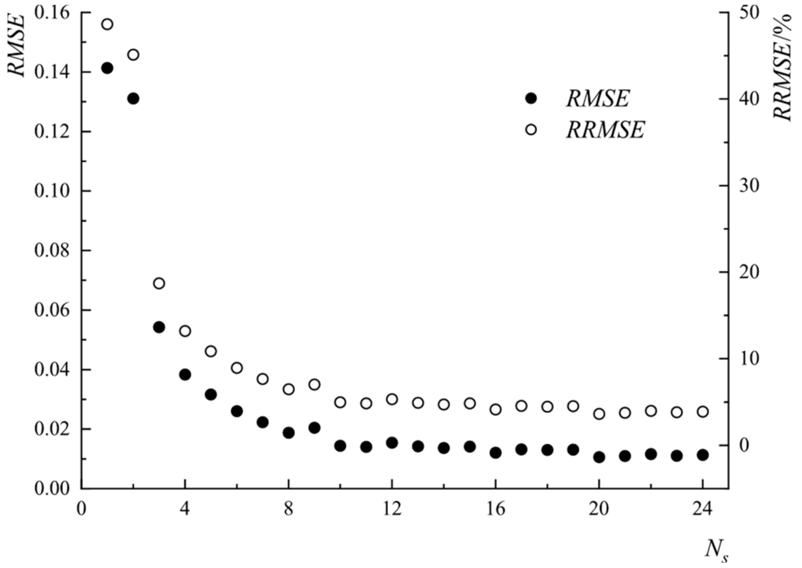

Figure 12. 3D pressure distribution reconstruction error of different numbers of sensors N_s.

Figure 13 shows the 3D pressure distribution reconstruction performance with different numbers of sensors. When $\delta_v = 0$, different numbers of sensors can all obtain good reconstruction results as the pressure is flat. When δ_v becomes larger, better pressure reconstruction results will be obtained with a larger number of sensors. When $N_s = 5$, the reconstructed pressure can roughly reflect the general distribution pattern of low pressure at the leading edge and high pressure at the trailing edge, but it is not capable of reconstructing the 3D pressure characteristics of the corners, as shown in Figure 13d,e. When $N_s = 15$, the leading edge 3D pressure feature can already be demonstrated (see Figure 13g,h). However, it cannot distinguish between the central 2D pressure and the 3D corner pressure. When $N_s = 24$, Figure 13j,k shows that the reconstructed pressure distribution characteristics are almost the same as that of the original ones shown in Figure 13a,b. Both the 2D pressure area and 3D corner area can be reconstructed well.

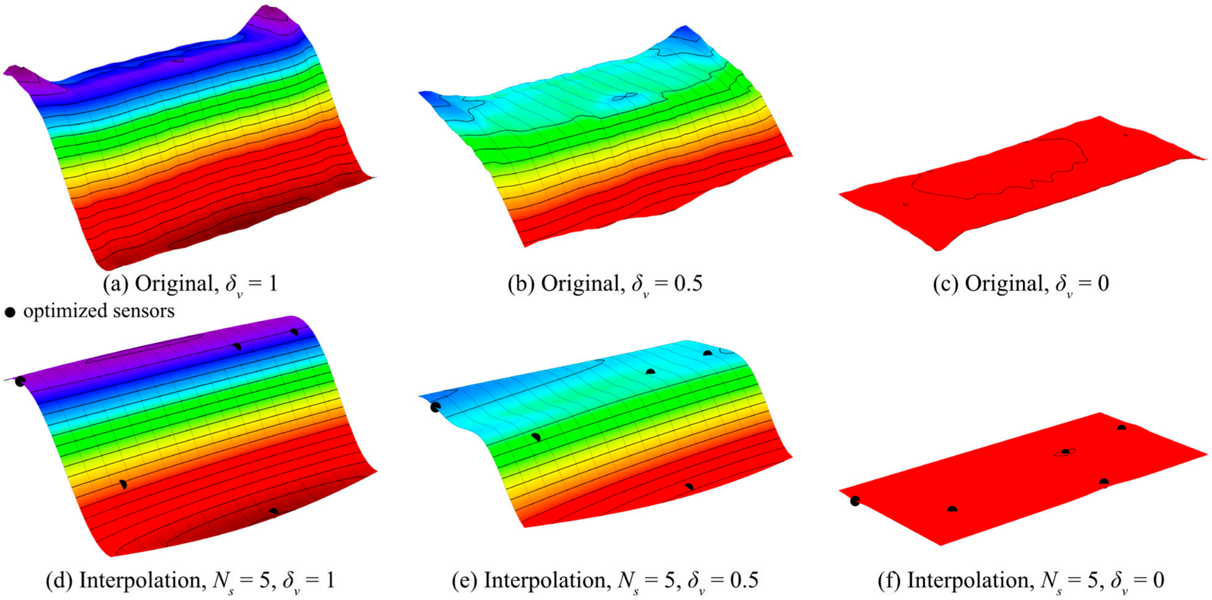

(a) Original, $\delta_v = 1$ (b) Original, $\delta_v = 0.5$ (c) Original, $\delta_v = 0$

(d) Interpolation, $N_s = 5$, $\delta_v = 1$ (e) Interpolation, $N_s = 5$, $\delta_v = 0.5$ (f) Interpolation, $N_s = 5$, $\delta_v = 0$

Figure 13. *Cont.*

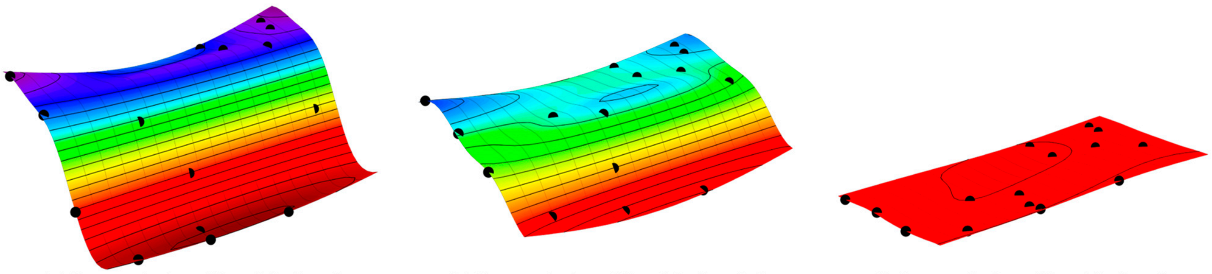

(g) Interpolation, $N_s = 15$, $\delta_v = 1$ (h) Interpolation, $N_s = 15$, $\delta_v = 0.5$ (i) Interpolation, $N_s = 15$, $\delta_v = 0$

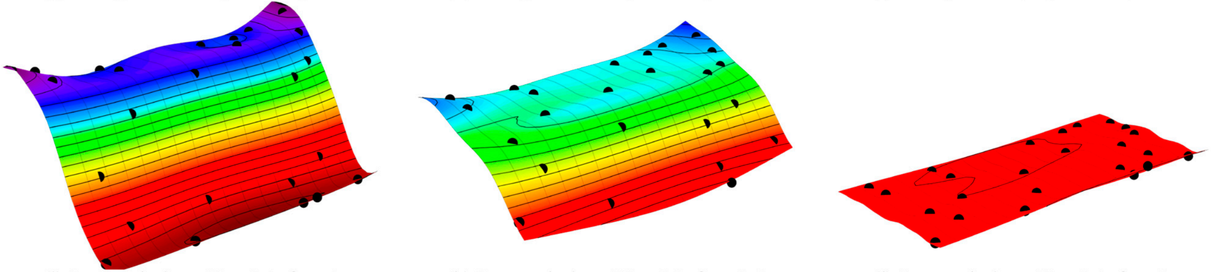

(j) Interpolation, $N_s = 24$, $\delta_v = 1$ (k) Interpolation, $N_s = 24$, $\delta_v = 0.5$ (l) Interpolation, $N_s = 24$, $\delta_v = 0$

Figure 13. 3D pressure distribution reconstruction results with different numbers of sensors.

With the reconstructed pressure distribution, the average wall pressure of a 3D jet is

$$\overline{C_p} = \frac{1}{WL}\iint C_p(x,y)dxdy, \tag{28}$$

where C_p (x, y) is the reconstructed 3D pressure distribution function.

4.3. Optimal Reconstruction of Half-3D Wall Pressure Distribution

If the jet transverse symmetry is used as a complementary condition, then it is possible to achieve a further reduction in sensor quantity while maintaining a good 3D pressure reconstruction performance. Assume that one sensor is located at P_1 (x_P, y_P); the pressure at P_1 possesses the following feature

$$C_p(x_P, y_P) = C_p(-x_P, y_P), \tag{29}$$

where C_p $(-x_P, y_P)$ is the pressure coefficient of point P_2 (x_P, y_P), which is symmetric with P_1 about the $\boldsymbol{y}$-axis.

Applying Equation (29), we can use N_s real sensors with N_s symmetrical virtual sensors to achieve measurement with $2 \times N_s$ sensors. We define this method as half-3D reconstruction. All real sensors are in the region where $x \geq 0$.

Figure 14 shows the half-3D pressure distribution reconstruction error of different N_s and the comparison of the half-3D method with the full-3D method. The two methods have the same error when N_s = 1. In addition to this, the half-3D method always has smaller pressure distribution reconstruction errors for all sensor quantities. This advantage is particularly evident at $2 \leq N_s \leq 9$, which brings about a significant error reduction.

The performance of half-3D pressure distribution reconstruction with different N_s is shown in Figure 15. When N_s = 5, the 3D corner pressure at the leading edge can already be roughly reconstructed, but the 2D area is poorly demonstrated, as shown in Figure 15d. When N_s = 15, Figure 15j,k shows that both the 2D pressure area and 3D corner area can be reconstructed well. Compared with the full-3D method in Figure 13, the half-3D method can achieve better 3D pressure reconstruction accuracy with fewer sensors.

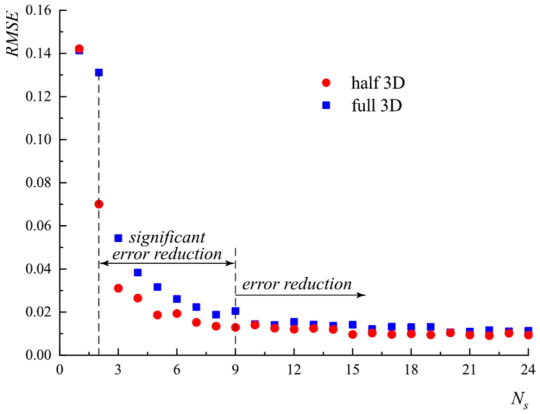

Figure 14. Half-3D pressure distribution reconstruction error of different numbers of sensors N_s.

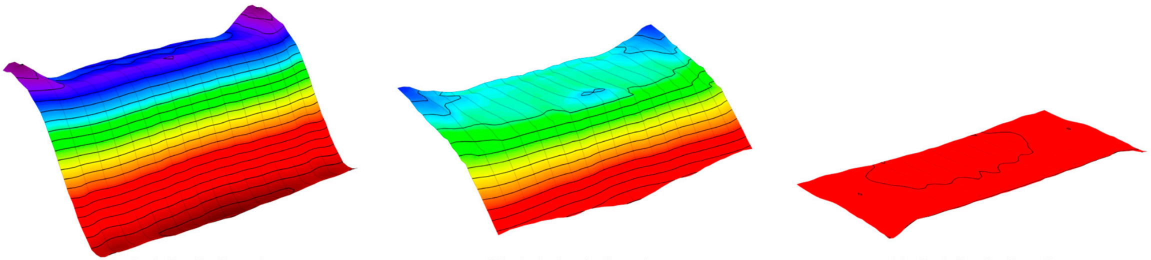

(a) Original, $\delta_v = 1$ (b) Original, $\delta_v = 0.5$ (c) Original, $\delta_v = 0$

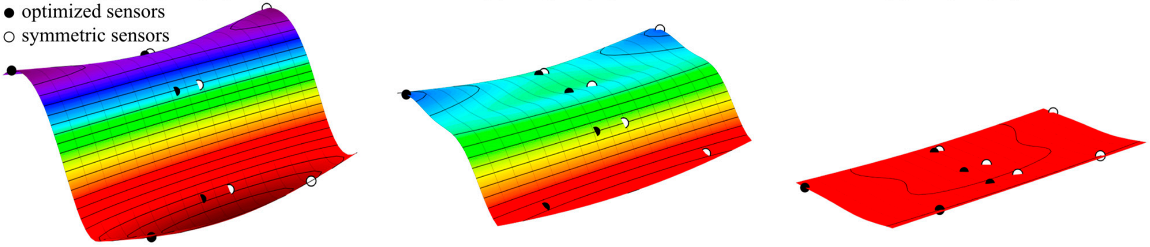

(d) Interpolation, $N_s = 5$, $\delta_v = 1$ (e) Interpolation, $N_s = 5$, $\delta_v = 0.5$ (f) Interpolation, $N_s = 5$, $\delta_v = 0$

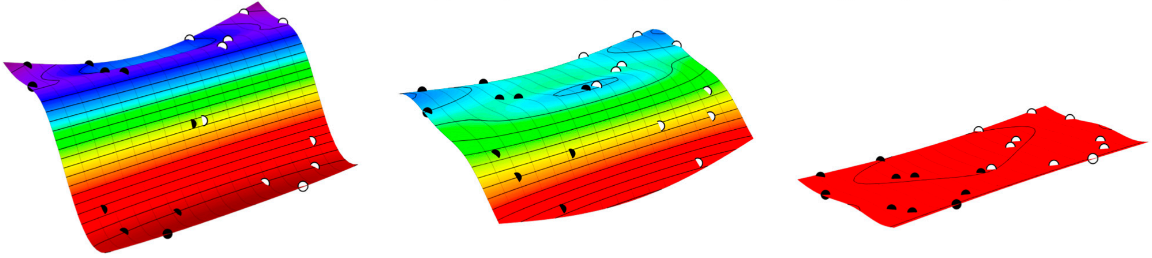

(g) Interpolation, $N_s = 10$, $\delta_v = 1$ (h) Interpolation, $N_s = 10$, $\delta_v = 0.5$ (i) Interpolation, $N_s = 10$, $\delta_v = 0$

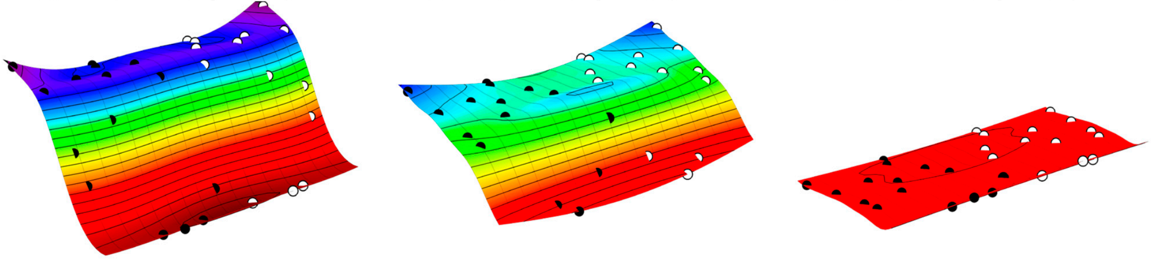

(j) Interpolation, $N_s = 15$, $\delta_v = 1$ (k) Interpolation, $N_s = 15$, $\delta_v = 0.5$ (l) Interpolation, $N_s = 15$, $\delta_v = 0$

Figure 15. Half-3D pressure distribution reconstruction results with different numbers of sensors.

For the half-3D method, the calculation of average wall pressure is the same as that of the full-3D method, as shown in Equation (28). We recommend the half-3D method rather than the full-3D method, and the case of N_s = 15 was taken for final verification.

4.4. Direct Average Pressure Method

The results presented in the previous sections are based on the pressure reconstruction method. According to Equation (14), it is the average wall pressure that needs to be obtained, and a completely accurate wall pressure distribution is not necessary. In this section, the average wall pressure is estimated directly by the average pressure of the sparse pressure sensors. The purpose of this method is to estimate the average wall pressure as accurately as possible with a minimum number of sensors. Figure 16 shows the error of the average pressure with different N_s. When $N_s \leq 2$, the estimation error of the average pressure is large. When $N_s \geq 3$, the error levels off. Based on the requirement to minimize the number of sensors, N_s = 3 was chosen as the preferred solution. For comparison, the case N_s = 1 is also verified in the next section.

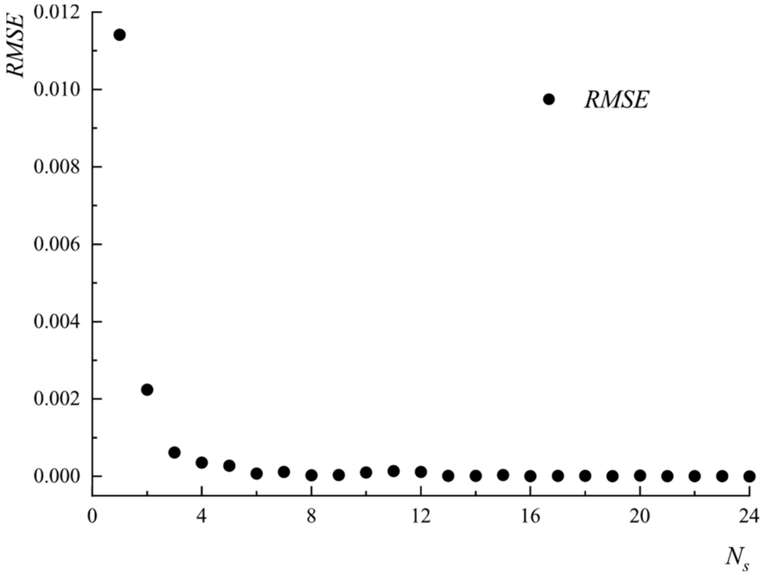

Figure 16. Error of average pressure with different numbers of sensors N_s.

With the direct average pressure method, the average pressure can be estimated by

$$\overline{C_p} = \frac{1}{N_s}\sum C_{pi}, i = 1, 2, \cdots, N_s. \tag{30}$$

4.5. Verification of the Thrust Vectoring Angle Estimation Method with Synchronous Experiments

4.5.1. Experimental Procedure

In the verification of our thrust vectoring angle estimation method, we used both balance force measurement and wall pressure measurement. The two types of data were collected synchronously on the timeline using an NI LabVIEW DAQ system. In the experiment, we first used the secondary flow valve to control the deflection of the jet. The balance measured the thrust vectoring angle θ_T directly, while the pressure transducers measured the wall pressure and indirectly estimated the thrust vectoring angle θ_P using the algorithm proposed in this investigation. Then, the accuracy of this thrust vectoring angle estimation method can be evaluated by comparing the errors between θ_T and θ_P.

4.5.2. Definition of the Sensor Arrays on the Verification Model

Synchronous force and pressure measurement experiments were carried out to verify the pressure-based thrust vectoring angle estimation method proposed in this research.

We set up 25 pressure measurement taps on the wall to verify four different estimation methods at the same time; the model is shown in Figure 17. The pressure measurement taps on the upper and lower walls are symmetrical about the ***XOY*** plane, with a total of 50 wall pressure sensors, as shown in Figure 1. The details of the sensor arrays are listed in Table 4.

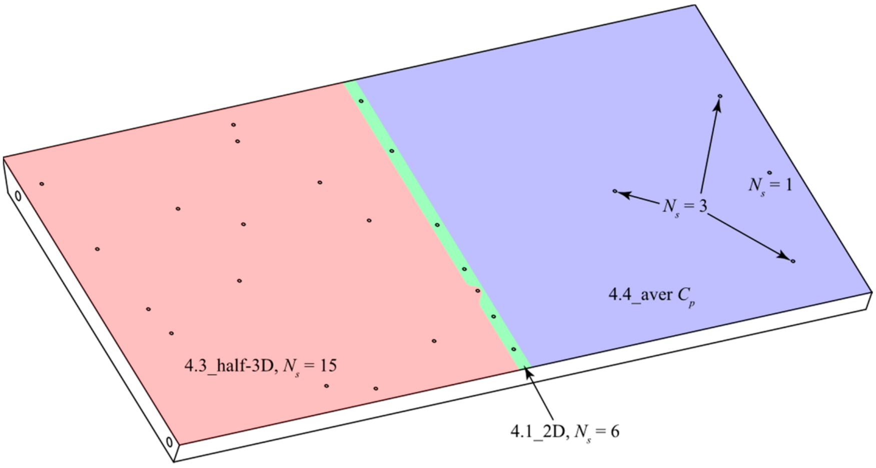

Figure 17. The optimized pressure sensor distributions in the verification model.

Table 4. Definition of the sensor arrays in the verification model.

No.	Method	N_s	Area (Figure 17)	Equations	Thrust Vectoring Angle Calculation Method
1	Balance	/	/	(4)	θ_T, Direct force measurement
2	4.1_2D	6	Green	(14) (26)	θ_P, Pressure-based estimation
3	4.3_half-3D	15	Pink	(14) (28)	
4	4.4_aver C_p	3	Blue	(14) (30)	
5		1			

4.5.3. Accuracy of Pressure-Based Thrust Vectoring Angle Estimation

The accuracy of pressure-based thrust vectoring angle estimation is verified by the control law of thrust vectoring angle with δ_v. During the experiment, the thrust vectoring angle is obtained in two different ways. The first is direct force measurement, whose result is θ_T. The second is a pressure-based estimation, whose result is θ_P. The calculating equations are summarized in Table 4. All of the thrust vectoring angles obtained by different methods are acquired synchronously in the same test.

From the control law shown in Figure 18a, it can be seen that θ_P estimated by the 2D method, half-3D method, and aver C_p_3 method agree well with θ_T. Figure 18b illustrates that the errors of the first three methods are small, their mean absolute errors ε are less than 0.5°, and their mean relative errors ε_r are less than 3.1%. However, the accuracy of the C_p_1 method, which uses only one sensor, is poor. The mean relative error is 17.5%. Note that the control law in Figure 18a shows a hysteresis loop between the jet attachment process and the jet detachment process; this is caused by the changes in the near-wall flow structures [31].

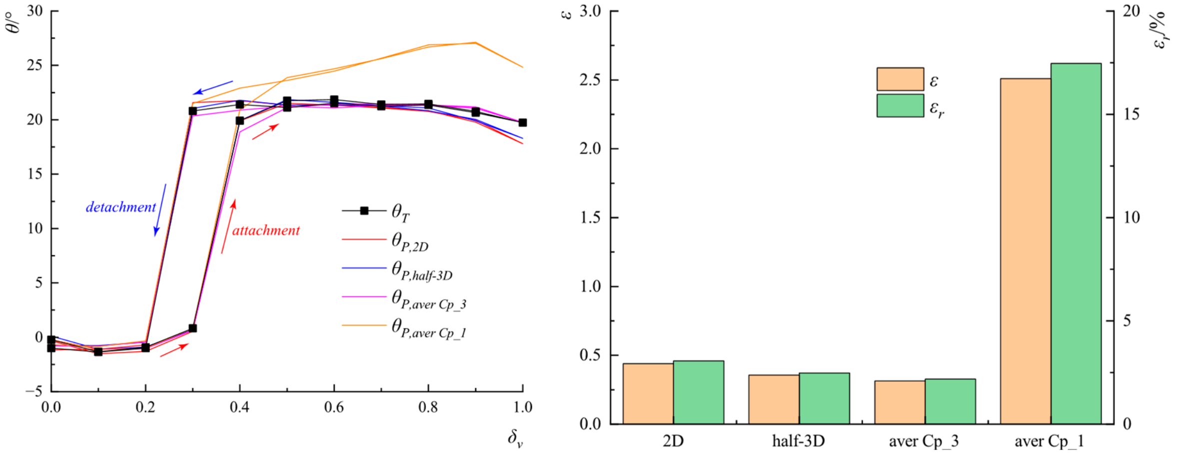

(**a**) (**b**)

Figure 18. The performance of the pressure-based thrust vectoring angle estimation. (**a**) Control law of thrust vectoring angle. (**b**) Thrust vectoring angle estimation error of the different methods.

Considering the objective of using the minimum number of sensors to achieve pressure-based thrust vectoring angle estimation, the direct average pressure method with N_s = 3 is a preferred solution. According to Equation (14), we need at least three *differential* sensors to acquire the pressure of the six measurement positions on the upper and lower walls.

4.5.4. Dynamic Response of Pressure-Based Thrust Vectoring Angle Estimation

In addition to accuracy, the pressure-based thrust vectoring angle estimation methods must possess good dynamic responses to meet the expectations in situations such as closed-loop feedback control, vehicle attitude control, etc. Take the half-3D method with N_s = 15 as an example; Figure 19a shows the synchronous dynamic response of θ_T and θ_P. During the test, the jet is initially in the neutral state. Then, multiple secondary flow valve closed–open switching is performed, whereupon the jet switches between attached and detached. The result shows that θ_T and θ_P maintain good consistency. A cross-correlation analysis is performed for θ_T and θ_P; Figure 19b shows that the normalized cross-correlation coefficient (NCC) reaches 0.99919 and that they remain synchronized in time. This suggests that the pressure-based thrust vectoring angle estimation has a good dynamic response capability.

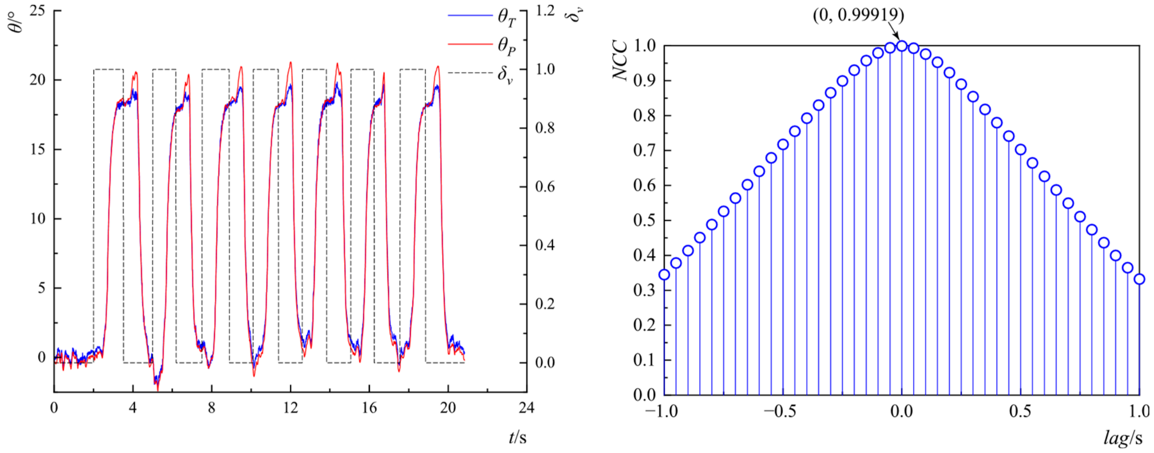

(**a**) (**b**)

Figure 19. The estimation performance of dynamic response. (**a**) The synchronous dynamic response of θ_T and θ_P. (**b**) The normalized cross-correlation of θ_T and θ_P.

4.5.5. Uncertainty Analysis

In our experiments, we performed seven independent repetitions of the balance measurement, as shown in Figure 20; in this section, we perform an uncertainty analysis for the thrust vectoring angle estimation method proposed in this paper.

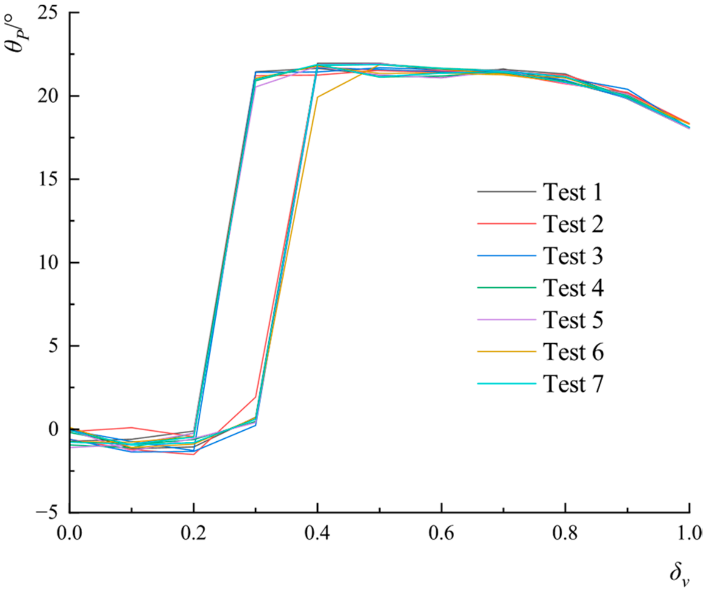

Figure 20. The seven independent repetitions of the balance measurement.

The type A evaluations of uncertainty u_A can be calculated by

$$u_A = \frac{s(x)}{\sqrt{n}} = \sqrt{\frac{1}{n(n-1)} \sum_{i=1}^{n} (x_i - \overline{x})^2}, \tag{31}$$

where $n = 7$ is the number of tests and $s(x)$ is the standard deviation.

According to Equation (31), the type A uncertainties of the thrust vectoring angle estimation method are summarized in Table 5.

Table 5. The type A uncertainties of the thrust vectoring angle estimation method.

Jet Attachment		Jet Detachment	
δ_v	u_A	δ_v	u_A
0	0.110°	1.0	0.048°
0.1	0.064°	0.9	0.044°
0.2	0.135°	0.8	0.061°
0.3	0.211°	0.7	0.042°
0.4	0.274°	0.6	0.074°
0.5	0.068°	0.5	0.078°
0.6	0.039°	0.4	0.090°
0.7	0.039°	0.3	0.119°
0.8	0.069°	0.2	0.146°
0.9	0.083°	0.1	0.146°
1.0	0.048°	0	0.147°

The above results show that a good estimation of thrust vectoring angle based on wall pressure can be achieved with a minimum of *three* differential pressure sensors. The half-3D method requires more sensors, but it can accurately reconstruct the overall wall pressure distribution. In the FTVC nozzles, the near-wall flow structures play a significant role in jet deflection control. Therefore, the half-3D method can assist in the study of the development of the near-wall 3D flow structures using the wall pressure distribution. Table 6 summarizes the different thrust vectoring angle estimation and wall pressure reconstruction methods and recommends their scope of application.

Table 6. Summary of different pressure-based thrust vectoring angle estimation methods and their recommended applications.

Method	Number of Sensors	Recommended for
2D	6	Wall pressure distribution reconstruction
Half-3D	15	
Direct average pressure	3	Real-time in-flight thrust vectoring angle estimation

5. Conclusions

We developed a pressure-based thrust vectoring angle estimation method for FTVC nozzles in this investigation. Multiple methods were proposed to reconstruct wall pressure distribution and estimate average wall pressure, including a 2D method, 3D method, half-3D method, and direct average pressure method. Non-dominated sorting genetic algorithm II was applied to find the optimal sensor arrays for reducing the sensor quantity. Synchronous force and pressure measurement experiments were carried out to verify the pressure-based thrust vectoring angle estimation methods. The most important findings are summarized as follows:

1. Direct average pressure method can provide a good estimation of thrust vectoring angle with a minimum of *three* differential pressure sensors;
2. The estimation method in this study is capable of accurate and fast response vectoring angle monitoring; the mean relative error is less than 3.1%;
3. The half-3D method requires more sensors, but it can accurately reconstruct the overall wall pressure distribution using a sparse array of pressure sensors, which is helpful in the study of the near-wall 3D flow structures in FTVC nozzles.

The pressure-based thrust vectoring angle estimation method proposed in this study has a good prospect for engineering applications; it is capable of real-time in-flight monitoring of the thrust vectoring angle with very few sensors. This method is extremely important and indispensable for the closed-loop feedback control and aircraft attitude control of FTVC technology.

This research proposed an accurate and practical pressure-based thrust vectoring angle estimation method. However, the accurate in-flight estimation of the thrust magnitude requires further study.

Author Contributions: Conceptualization, N.S. and Y.G.; methodology, N.S. and Y.G.; software, T.W.; validation, Y.G.; investigation, N.S., Y.Z., Y.W. and S.D.; resources, Y.Z.; data curation, N.S. and T.W.; writing—original draft preparation, N.S. and T.W.; writing—review and editing, Y.G., Y.Z., Y.W. and S.D.; visualization, N.S.; funding acquisition, Y.G. All authors have read and agreed to the published version of the manuscript.

Funding: This research was funded by the National Natural Science Foundation of China grant number 11972017, and the Priority Academic Program Development of Jiangsu Higher Education Institutions.

Data Availability Statement: Data are contained within the article.

Conflicts of Interest: We declare that no conflict of interest exists in the submission of this manuscript and that the manuscript is approved by all authors for publication. We do not have any commercial or associative interests that represent a conflict of interest in connection with the work submitted.

Nomenclature

$C_p, \overline{C_p}$	Pressure coefficient and average pressure coefficient
DAQ	Data acquisition
FTVC	Fluidic thrust vectoring control
G	Offset of the secondary flow channel
H	Height of the jet outlet
L	Length of the inclined wall
N_i	Times of iterations
N_s	Number of sensors
NSGA-II	Non-dominated sorting genetic algorithm II
RMSE	Root mean square error
RRMSE	Relative root mean square error
TVC	Thrust vectoring control
u_{A}	Type A evaluations of uncertainty
v_∞	Velocity of the jet at the outlet
W	Width of the jet outlet
$\boldsymbol{x}$, $\boldsymbol{y}$	Axes of the wall coordinate system
x_P, y_P	Coordinates of point P in the wall coordinate system
$\boldsymbol{X}$, $\boldsymbol{Y}$, $\boldsymbol{Z}$	Axes of the nozzle coordinate system
x^*, x_{real}	Measured value and real value
δ_v	Closure percentage of the secondary flow valve
ε, ε_r	Mean absolute error and mean relative error
θ	Incline angle of the inclined wall
θ_P	Thrust vectoring angle estimated by wall pressure
θ_T	Thrust vectoring angle
ρ	Density of air
2D, 3D	Two-dimensional, three-dimensional

References

1. Waithe, K.A.; Deere, K. Experimental and computational investigation of multiple injection ports in a convergent-divergent nozzle for fluidic thrust vectoring. In Proceedings of the 21st AIAA Applied Aerodynamics Conference, Orlando, FL, USA, 23–26 June 2003. AIAA Paper 2003-3802. [CrossRef]
2. Lian, Y.J. Fluidic thrust vectoring techniques research. *Aircr. Des.* **2008**, *28*, 19–24. (in Chinese). [CrossRef]
3. Wing, D.J. Static Investigation of Two Fluidic Thrust-Vectoring Concepts on a Two-Dimensional Convergent-Divergent Nozzle. NASA TM-4574. 1994. Available online: https://ntrs.nasa.gov/citations/19950012627 (accessed on 16 October 2022).
4. Wu, K.X.; Kim, H.D. Numerical study on the shock vector control in a rectangular supersonic nozzle. *J. Aerosp. Eng.* **2019**, *233*, 4943–4965. [CrossRef]
5. Shi, J.W.; Wang, Z.X.; Zhou, L.; Zhang, X.B. Numerical investigation on a new concept of shock vector control nozzle. *J. Eng. Gas Turbines Power* **2019**, *141*, 091004. [CrossRef]
6. Miller, D.N.; Yagle, P.J.; Hamstra, J.W. Fluidic Throat skewing for thrust vectoring in fixed geometry nozzles. In Proceedings of the 37th aerospace sciences meeting and exhibit, Reno, NV, USA, 11–14 January 1999. AIAA Paper 99-0365. [CrossRef]
7. Williams, R.G.; Vittal, B.R. Fluidic thrust vectoring and throat control exhaust nozzle. In Proceedings of the 38th AIAA/ASME/SAE/ASEE Joint Propulsion Conference & Exhibit, Indianapolis, Indiana, 7–10 July 2002. AIAA Paper 2002-4060. [CrossRef]
8. Wang, Y.S.; Xu, J.L.; Huang, S.; Lin, Y.C.; Jiang, J.J. Computational study of axisymmetric divergent bypass dual throat nozzle. *Aerosp. Sci. Technol.* **2019**, *86*, 177–190. [CrossRef]
9. Wang, Y.S.; Xu, J.L.; Huang, S.; Jiang, J.J.; Pan, R.F. Design and preliminary analysis of the variable axisymmetric divergent bypass dual throat nozzle. *J. Fluids Eng.* **2020**, *142*, 061204. [CrossRef]
10. Huang, S.; Xu, J.L.; Yu, K.K.; Wang, Y.S.; Pan, R.F. Design and experimental study of a bypass dual throat nozzle with the ability of short/vertical takeoff and landing. *Aerosp. Sci. Technol.* **2022**, *121*, 107301. [CrossRef]
11. Wu, K.X.; Kim, H.D.; Jin, Y. Fluidic thrust vector control based on counter-flow concept. *Proc. Inst. Mech. Eng. Part G* **2018**, *223*, 1412–1422. [CrossRef]
12. Wu, K.X.; Kim, T.H.; Kim, H.D. Sensitivity analysis of counterflow thrust vector control with a three-dimensional rectangular nozzle. *Proc. Inst. Mech. Eng. Part G* **2021**, *34*, 04020107. [CrossRef]
13. Mason, M.S.; Crowther, W.J. Fluidic thrust vectoring for low observable air vehicles. In Proceedings of the 2nd AIAA Flow Control Conference, Portland, OR, USA, 28 June–1 July 2004. AIAA Paper 2004-2210. [CrossRef]

14. Wen, X.; Zhou, K.W.; Liu, P.C.; Zhu, H.J.; Wang, Q.; Liu, Y.Z. Schlieren visualization of coflow fluidic thrust vectoring using sweeping jets. *AIAA J.* **2022**, *60*, 435–444. [CrossRef]
15. Shi, N.X.; Gu, Y.S.; Zhou, Y.H.; Wang, Y.; Li, Z. Experimental investigation on the transient process of jet deflection controlled by passive secondary flow. *J. Visualization.* **2022**, *25*, 967–981. [CrossRef]
16. Gong, D.S.; Gu, Y.S.; Zhou, Y.H.; Shi, N.X. Control law of passive fluid thrust vector nozzle based on thermal jet of micro turbojet engine. Acta Aeronaut. *Astronaut. Sin.* **2020**, *41*, 106–117. (in Chinese). [CrossRef]
17. Flamm, J.D. Experimental study of a nozzle using fluidic counterflow for thrust vectoring. In Proceedings of the 34th AIAA/ASME/SAE/ASEE Joint Propulsion Conference and Exhibit, Cleveland, OH, USA, 13–15 July 1998. AIAA Paper 98-3255. [CrossRef]
18. Anzalotta, C.; Joshi, K.; Fernandez, E.; Bhattacharya, S. Effect of forcing the tip-gap of a NACA0065 airfoil using plasma actuators: A proof-of-concept study. *Aerosp. Sci. Technol.* **2020**, *107*, 106268. [CrossRef]
19. Raman, G.; Packiarajan, S.; Papadopoulos, G.; Weissman, C.; Raghu, S. Jet thrust vectoring using a miniature fluidic oscillator. *Aeronaut. J.* **2005**, *109*, 129–138. [CrossRef]
20. Bauer, M.; Friedrichs, J.; Wulff, D.; Werner-Spatz, C. Development and Validation of an On-Wing Engine Thrust Measurement System. American Society of Mechanical Engineers: New York, NY, USA, 2017; ASME GT2017-63277. [CrossRef]
21. Johansen, E.S.; Rediniotis, O.K.; Jones, G. The compressible calibration of miniature multi-hole probes. *J. Fluids Eng.* **2001**, *123*, 128–138. [CrossRef]
22. Burelle, L.A.; Yang, W.C.; Rival, D.E. *From Sparse Pressure Measurements to Prediction of Instantaneous Loads: A Test Case on Delta Wings in Axial and Transverse Gusts*; AIAA SciTech Forum: Orlando, FL, USA, 6–10 January; 2020; AIAA Paper 2020–2044. [CrossRef]
23. Whitmore, S.A.; Cobleigh, B.R.; Haering, E.A. Design and calibration of the X-33 flush airdata sensing (FADS) system. In Proceedings of the 36th AIAA Aerospace Sciences Meeting and Exhibit, Reno, Nevada, USA, 1998, 12–15 January. AIAA Paper 98-0201. [CrossRef]
24. Wang, Q.T.; Cheng, K.M.; Gu, Y.S.; Li, Z.Q. Continuous control of asymmetric forebody vortices in a bi-stable state. *Phys. Fluids* **2018**, *30*, 024102. [CrossRef]
25. Zaitsev, E.G. Investigation of the propagation of a two-dimensional wall jet over a step. *Fluid Dyn.* **1991**, *26*, 526–530. [CrossRef]
26. Smith, B.L.; Glezer, A. Jet vectoring using synthetic jets. *J. Fluid Mech.* **2002**, *458*, 1–34. [CrossRef]
27. Gillgrist, R.D.; Forliti, D.J.; Strykowski, P.J. On the mechanisms affecting fluidic vectoring using suction. *J. Fluids Eng.* **2007**, *129*, 91–99. [CrossRef]
28. Bourque, C.; Newman, B.G. Reattachment of a two-dimensional, incompressible jet to an adjacent flat plate. *Aeronaut. Q.* **1960**, *11*, 201–232. [CrossRef]
29. Lai, J.C.S.; Lu, D. Effect of wall inclination on the mean flow and turbulence characteristics in a two-dimensional wall jet. *Int. J. Heat Fluid Flow.* **1996**, *17*, 377–385. [CrossRef]
30. Driver, D.M.; Seegmiller, H.L. Features of a reattaching turbulent shear layer in divergent channel flow. *AIAA J.* **1985**, *23*, 163–171. [CrossRef]
31. Shi, N.X.; Gu, Y.S.; Zhou, Y.H.; Wang, L.X.; Feng, C.; Li, L.K. Mechanism of hysteresis and uncontrolled deflection in jet vectoring control based on Coanda effect. *Phys. Fluids* **2022**, *34*, 084107. [CrossRef]
32. Holland, J.H. Genetic algorithms and the optimal allocation of trials. *SIAM J. Comput.* **1973**, *2*, 88–105. [CrossRef]
33. Lambora, A.; Gupta, K.; Chopra, K. Genetic algorithm—A literature review. In Proceedings of the 2019 International Conference on Machine Learning, Faridabad, India, 14–16 February 2019; pp. 380–384. [CrossRef]
34. Hu, Y.; Sun, Z.S.; Cao, L.J.; Zhang, Y.; Pan, P.F. Optimization configuration of gas path sensors using a hybrid method based on tabu search artificial bee colony and improved genetic algorithm in turbofan engine. *Aerosp. Sci. Technol.* **2021**, *112*, 106642. [CrossRef]
35. Gong, X.L.; Zheng, X.R.; Fang, J.C.; Liu, G. Optimized layout methods based on optimization algorithms for DPOS. *Aerosp. Sci. Technol.* **2019**, *84*, 484–496. [CrossRef]
36. Cuadrado, D.G.; Marconnet, A.; Paniagua, G. Inverse conduction heat transfer and kriging interpolation applied to temperature sensor location in microchips. *J. Electron. Packag.* **2018**, *140*, 010905. [CrossRef]
37. Norouzi, A.; Zaim, A.H. Genetic algorithm application in optimization of wireless sensor networks. *Sci. World J.* **2014**, *2014*, 286575. [CrossRef]
38. Sun, Y.L.; Zhang, C.; Ji, H.L.; Qiu, J.H. A temperature field reconstruction method for spacecraft leading edge structure with optimized sensor array. *J. Intell. Mater. Syst. Struct.* **2021**, *32*, 2024–2038. [CrossRef]
39. Srinivas, N.; Deb, K. Muiltiobjective optimization using nondominated sorting in genetic algorithms. *Evol. Computation* **1994**, *2*, 221–248. [CrossRef]
40. Deb, K.; Pratap, A.; Agarwal, S.; Meyarivan, T. A fast and elitist multiobjective genetic algorithm: NSGA-II. *IEEE Trans. Evol. Comput.* **2002**, *6*, 182–197. [CrossRef]
41. Cai, Y.; Rajaram, D.; Mavris, D.N. Simultaneous aircraft sizing and multi-objective optimization considering off-design mission performance during early design. *Aerosp. Sci. Technol.* **2022**, *126*, 107662. [CrossRef]
42. Strykowski, P.J. An Experimental/Modeling Study of Jet Attachment during Counterflow Thrust Vectoring. NASA CR-204436. 1997. Available online: https://ntrs.nasa.gov/citations/19970018356 (accessed on 17 October 2022).

43. Ghorbani, M.A.; Shamshirband, S.; Haghi, D.Z.; Azani, A.; Bonakdari, H.; Ebtehaj, I. Application of firefly algorithm-based support vector machines for prediction of field capacity and permanent wilting point. *Soil Tillage Res.* **2017**, *172*, 32–38. [CrossRef]
44. Aumond, P.; Can, A.; Mallet, V.; Coensel, B.D.; Ribeiro, C.; Botteldooren, D.; Lavandier, C. Kriging-based spatial interpolation from measurements for sound level mapping in urban areas. *J. Acoust. Soc. Am.* **2018**, *143*, 2847–2857. [CrossRef] [PubMed]
45. Belkhiri, L.; Tiri, A.; Mouni, L. Spatial distribution of the groundwater quality using kriging and Co-kriging interpolations. *Groundw. Sustain. Dev.* **2020**, *11*, 100473. [CrossRef]
46. Matheron, G. Principles of geostatistics. *Econ. Geol.* **1963**, *58*, 1246–1266. [CrossRef]
47. Krige, D.G. A statistical approach to some basic mine valuation problems on the Witwatersrand. *J. South. Afr. Inst. Min. Metall.* **1951**, *52*, 119–139.
48. Trangmar, B.B.; Yost, R.S.; Uehara, G. Application of geostatistics to spatial studies of soil properties. *Adv. Agron.* **1986**, *38*, 45–94. [CrossRef]
49. Cressie, N.A.C. *Statistics for Spatial Data*; John Wiley & Sons: New York, NY, USA, 1993.
50. Zhang, Q.Y.; Wu, J.T. Image super-resolution using windowed ordinary Kriging interpolation. *Opt. Commun.* **2015**, *336*, 140–145. [CrossRef]